Numerical Heat Transfer, Part A: Applications, Vol. 64, Issue 4, pp. 290-316, 2015.

On the transient numerical modelling of impinging jets heat transfer

Abstract

This work compares a number of CFD transient models of an impinging jet. The specific case considered is an impinging jet with z/D = 6 and Re 23000. The variables tested are: Turbulence model (LES, k-ε, V2F and DES), discretization schemes, mesh density and topology and influence of inlet turbulence for a total of 15 simulations. The comparison is based on the heat transfer prediction compared with experiments, resolved and modelled turbulent kinetic energy upstream of the impingement wall and the computational cost. It is found that the turbulence created in the shear layer plays a stronger role than the inlet turbulence. The LES model reproduces the behavior of turbulent structures with a useful degree of accuracy; the LES, DES and V2F models are capable of accurately predicting heat transfer to the impingement wall.

Key words: impinging jet, heat transfer, CFD, LES, V2F.

Abbreviations

μ molecular viscosity (kg/ m^2s)	u', v', w': velocity fluctuation (m/s)
μ_t turbulent viscosity (kg/ m^2s)	W_b: bulk inlet velocity (m/s)
const: constant	y^+ dimensionless wall distance
D: diameter (m)	z: height (m)
h heat transfer coefficient (W/m^2K)	ε turbulence dissipation rate (m^2/s^3)
k thermal conductivity (W/mK)	θ: angle (rad or deg)
k: (specific) turbulent kinetic energy (m^2/s^2)	CFD Computational Fluid Dynamics
l turbulent length scale (m)	CPU Central Processing Unit
Nu Nusselt number	DES Detached Eddy Simulation
r: radius (m)	ICE internal combustion engine
Re Reynolds number	LES Large Eddy Simulation
U, V, W: average velocity (m/s)	rms root mean squared
u, v, w: velocity (m/s)	RANS Reynolds Averaged Navier-Stokes

Table of contents

1 Introduction

Impinging jets flows have remarkable features and find many applications in industry. Consequently, this type of flow has been object of interest for many researchers. However, part of the physics governing impinging jet flows is not fully understood and this prevents a satisfying prediction of the effects of an arbitrary jet configuration.

A particularly interesting aspect of impinging jets is the heat transfer occurring between the fluid and the wall. The convective phenomena give rise to the highest levels of heat transfer coefficient known for single phase flows. Moreover, the heat transfer is strongly dependent on the position relative to the stagnation point.

Impinging jets have been studied in a number of configurations varying in geometrical and dynamic parameters. The dynamic variables basically are related to the jet velocity and the level of turbulence in the flow [3, 5, 6, 9, 11].

Impinging jets have been historically studied analytically and experimentally. Later, numerical simulations have also been deployed in this field. Numerical simulations are nowadays an established method to study and predict fluid flows. Therefore, they are widely used for product development in industry. Attempts to study impinging jets have been carried out using CFD (Computational Fluid Dynamics) simulations with varying degrees of success [7, 14, 15, 16, 18]. The general conclusion is that the more detailed the model the better it can capture the flow feature. However, detailed models are increasingly computationally expensive and have bigger stability problems. When considering industrial applications it is important to consider also these latter factors.

Reference [14], by the author of this work, addresses impinging jets with a steady state (time averaged) approach. In [14] it was concluded that transient phenomena can play an important role in the impingement process even if the flow is stationary. The present work extends the study with a transient analysis of stationary impinging jets. It compares the performance of different modelling parameters, including different turbulence models. The evaluation is not only based on the comparison with experimental data but also on the computational effort necessary to perform the simulation.

2 Impinging jet physics

2.1 Impinging jet flow features

A comprehensive description of impinging jets is presented in [10, 11]. Here a short description is given, in order to bring attention to some important features relevant to the present work. An impinging jet is characterized by a jet flow impacting (impinging) on a surface. The resulting flow field can be divided in 3 regions (see Figure 1).

- The *free jet region* in which the wall is not affecting the flow field. This region can be further sub-divided in two. 1) The potential core where the flow basically maintains its initial velocity (nozzle outlet velocity). 2) The shear layer where the jet interacts with the surrounding medium exchanging momentum and mass.

- In the *impinging region* the flow strikes to the wall and is forced to undergo a sudden change of direction. The stagnation point is located at the centre of this region.
- The *wall jet region* in which the flow leaving the impinging region develops into a semi-confined flow.

In the jet shear layer large parallel toroidal (donut-like) vortices interact with each other. Under certain flow conditions the vortices merge in an event called "vortex pairing" (see Figure 1), this is a case of turbulence back scattering. Back scattering is the transfer of turbulent kinetic energy from small to larger turbulent length scales. This is a known phenomenon typical of certain turbulent flows and it presents a difficulty for common turbulence models, which are designed assuming turbulence to be purely dissipative.

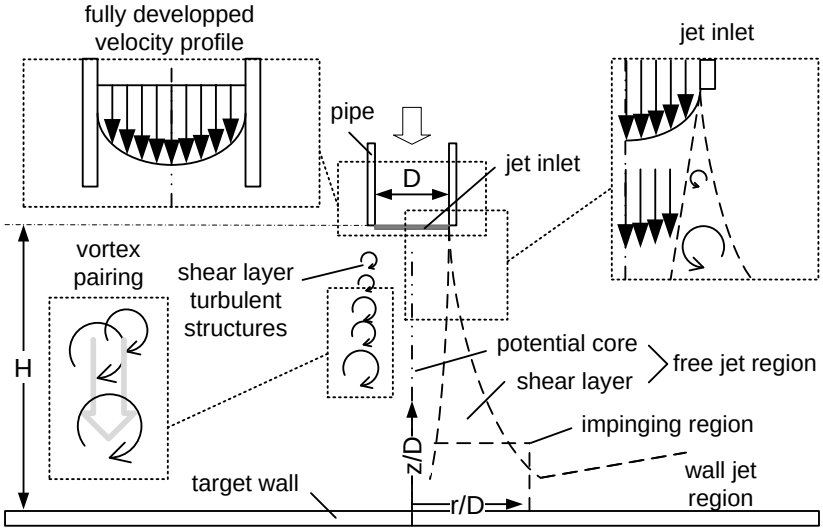

Figure 1. Physical processes in impinging jets.

Impinging jet flow has remarkable effects on convective heat transfer. Indeed, this kind of flow has among the highest known levels of Nusselt number (Nu) for single phase flows.

There are different types and configurations of impinging jets. A distinction can be made by the shape of the nozzle (circular, slot, or square), the upstream flow can be fully or partially developed and the jet may be confined by an upper wall. Unless otherwise stated, in this work *impinging jet* refers to a fully developed turbulent flow discharged from a circular pipe without confinement and orthogonally impinging a flat surface. The jet is discharged in a quiescent (still) medium of the same nature as the jet flow.

The nozzle diameter D is the reference length to characterize jet flows. The most important parameters to describe impinging jets heat transfer are the two dimensionless groups Nusselt Number (Nu) and Reynolds number (Re). Geometrical parameters are the nozzle to wall spacing (z/D) and the radial position (r/D). Another important parameter is the inlet turbulence intensity. The final goal of the research on impinging jets is to understand the physics governing the phenomenon and correlate all these parameters.

2.2 Impinging jet heat transfer

An example of experimental results is proposed in Figure 2. The Nusselt number presents a maximum at the stagnation point. Here the boundary layer thickness is at its minimum, offering the minimum resistance to the heat flux. The Nu then tends to decrease for grater r/D due to the growth of the boundary layer. Moreover, the radial flow velocity decreases as the flow spreads to an increasingly larger area.

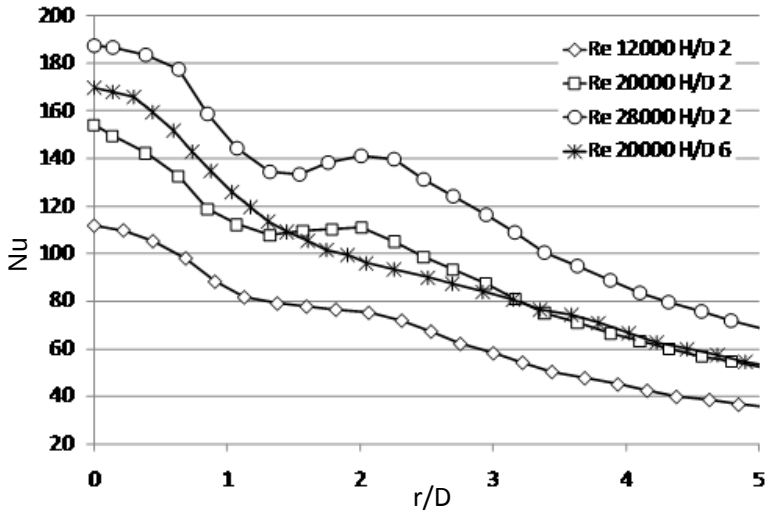

Figure 2. Experimental results Nu(r/D) [2].

For relatively high Re and small z/D (e.g. Re = 30000 and z/D = 2) the Nusselt number Nu(r/D) presents a secondary peak (Figure 2). This phenomenon is not fully understood despite considerable experimental and numerical efforts [4, 5, 6, 8].

Various explanations are suggested to explain the characteristic secondary peak. One reason is as follows: the free jet feeds the wall jet region as a column of fluid as shown in Figure 3. In the impingement region the flow diverges in radial direction forcing it to a strong angular acceleration creating the wall jet region. Strong acceleration holds the boundary layer laminar damping velocity fluctuations normal to the flow. Moreover, in the acceleration zone, the flow is pressed against the wall by the incoming column of fluid. The acceleration results in high velocity which in turn generates high heat transfer. As the radial distance increases, the velocity decreases because the cross-sectional area of the flow in the wall jet region increases.

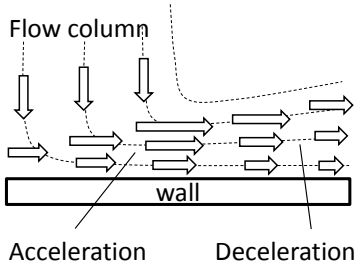

Figure 3. The acceleration-deceleration effect.

An alternative explanation relates to the development of the boundary layer. The laminar boundary layer develops from the stagnation point and eventually undergoes the transition to turbulent flow. The transition region is associated with an increase in heat transfer due to the enhancement of mass transfer in the direction normal to the wall. This transition can be associated to the secondary peak in the Nu(r/D). The boundary layer development for an impinging jet is different from the one of a flat plate. An important difference is the radial flow velocity decreases due to the radial increase of the cross-section area.

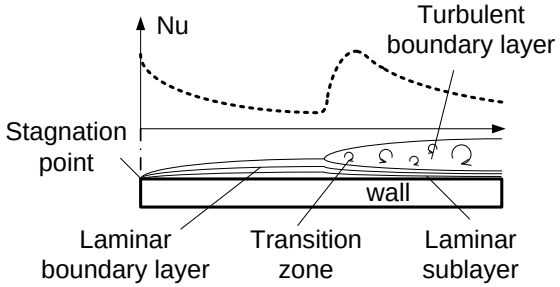

Figure 4. Effects of the development of the boundary layer on Nu (qualitative).

A third explanation for the secondary peak is that turbulent vortices grow in the shear layer of the free jet. These structures travel in the jet direction and impact on the target surface in a ring around the impingement point. The resulting velocity fluctuations normal to the wall increase the heat transfer affecting the boundary layer structure. This theory is supported by measurements [5, 6] correlating the vortices frequency with the fluctuation of the heat transfer rate.

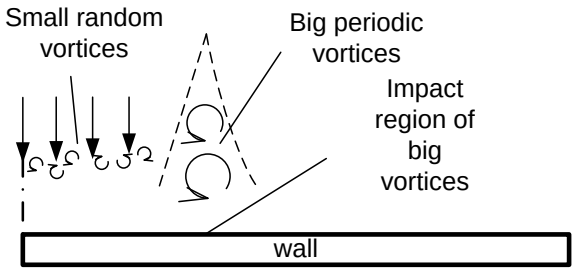

Figure 5. Shear layer vortex wall impact.

It is likely that the secondary peak in the Nusselt number curve is attributable to same combination of the three effects presented above. Interestingly, for very small values of z/D a third peak is observed, suggesting that the different phenomena act at different locations [10].

The heat transfer rate depends on the jet inlet conditions such as the velocity profile at the nozzle. Another important parameter is the turbulence intensity. High levels of turbulence enhance the momentum diffusion of the jet and consequently reduce the potential core length. The effect of the turbulence is strong enough to eliminate the local minimum occurring for high Re and small z/D. However, this variable has a lower impact for higher z/D where the turbulence created in the shear layer becomes dominant [10, 11].

3 Modelling of impinging jets

3.1 Modelling methodology

A CFD model is a complex assembly of a number of interacting sub-models (e.g. turbulence model, numerically discretization). The choice of these sub-parts influences the final result. In this study a number of variables are tested and cross compared in order to serve as a future reference for setting up an efficient simulation for impinging "jet - like" flows. This section discusses each of the different parts of the model individually.

3.1.1 Time (temporal discretization)

The characteristics of a stationary jet can be meaningfully represented by a time-averaged solution. However, by resolving also the time variation of the flow it is possible to gain a deeper understanding of the phenomena governing the impinging jet. It is also known that some problems related to simulation stability can be overcome by running a transient simulation of a stationary problem. The downside of this approach is that it significantly increases the simulation's computational cost. An important parameter in transient simulations is the CFL number, which is defined as

$$CFL = \frac{u\Delta t}{\Delta x}$$

Here, u is the generic velocity, Δt is the time step and Δx is the cell size in the u direction. Physically, this quantity defines how many cells a fluid particle passes through in a time step. For a robust transient simulation the CFL should be smaller than one but for practical reasons, a larger CFL number is often tolerated. In this project the simulation time step is chosen so that the CFL number is around one for most of the domain, allowing temporary local maxima of about ten.

3.1.2 Space (spatial discretization)

Figure 6 provides an overview of the geometry along with details of the mesh and boundary conditions. The mesh defines how the computational domain is discretized. The geometry is divided in 100 layers in direction normal to the impingement plane. The size of the cell layer closest to the impingement wall is chosen so that $y^+<1$ is satisfy in every location. This condition is necessary to resolve the viscous sub-layer (see zoom-in in Figure 6). The circular shape of the domain is discretized using the "peacock" topology. This topology allows for a flexible increase in the number of cells in both the radial and the angular directions and gives better results than the more commonly used "o-grid" topology [15]. Three meshes are created respectively with a total of 0,125, 0,5 and 2 million cells.

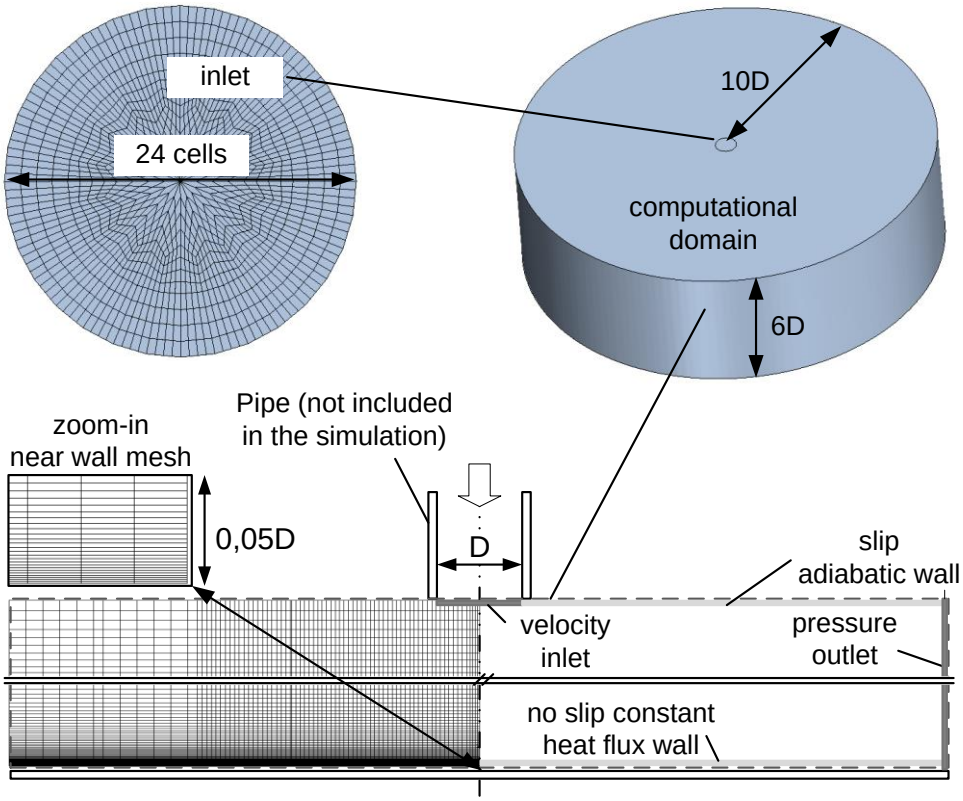

Figure 6. Computational domain, mesh and boundary conditions.

3.1.3 Inlet, outlet and wall boundary conditions

The outlet boundary condition is *pressure* (see Figure 6). The upper boundary condition is *slip wall. Pressure* would be a better boundary condition for the upper wall but this condition is avoided being more prone to numerical instability. This choice is backed by the measurements in [8] showing negligible differences in heat transfer between confined and unconfined jets for $z/D \geq 2$. The boundary condition on the impingement wall is *no slip wall* with a constant heat flux, reproducing an electrical resistor as in the experiments.

The inlet boundary condition is set as *velocity inlet*. The velocity profile for a fully developed pipe-flow is calculated in a separate simulation and mapped at the inlet boundary. In the finer mesh, the inlet boundary is discretized with 1280 cells (see Figure 6). This resolution is fine enough to resolve the biggest turbulent structures of the inlet flow. Synthetic turbulent fluctuations are superimposed to the fully developed turbulent profile.

3.1.4 Inlet synthetic turbulent fluctuations

The turbulent fluctuations are calculated using the method presented in [12], only a brief overview is provided in this section. The method is specifically design to generate inlet boundary conditions to LES (Large Eddy Simulation) and DES (Detached Eddy Simulation). The turbulent integral length scale and time scale are derived from the inlet

size and Reynolds number. A number of independent synthetized velocity fields are produced based on the turbulent integral length scale. The fields are independent in the sense that their time correlation is zero. When running the simulation, one of the computed velocity fields is superimposed as initial conditions for the inlet. The inlet condition for a given time step *N* is calculated as a weighted average between the fluctuation field *N* and the superimposed fluctuation field at *N*-1, this latter being function of all previously used fields. This interpolation is called an "asymmetric time filter" and is a function of the turbulent integral time scale and the simulation time step. From the above description it follows that to calculate the inlet conditions at a given time step it is necessary to retrieve the inlet conditions at the previous time step.

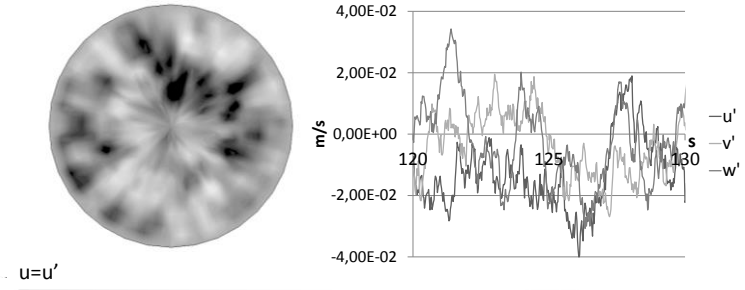

Figure 7. Example of synthetic fluctuations superimposed at the inlet. Instantaneous inlet u' field and time resolved fluctuations in one inlet boundary cell.

The result of the application of the method presented above is a space and time correlated field of the velocity fluctuations at the inlet. Figure 7 shows an example of these fluctuations. It can be noticed as the three fluctuation components are of the same order of magnitude. Consequently, at the inlet the cell aspect ratio should be about one to properly resolve the fluctuations.

3.1.5 Equations (numerical discretization)

The simulations are carried out using STAR-CD. This commercial code can be run with its own patented discretization scheme called MARS. This is a second order discretization scheme. The MARS ability to capture strong gradients in the flow can be changed by using different setting for the scheme's compression level. This can be changed between 0 and 1. Low values for this parameter result in a more robust model, less prone to diverge or crash. With higher values of this parameter the simulation is able to capture more accurately sharp gradients in the flow field. The default value for this parameter is 0,5 which is a compromise between accuracy and robustness. The same differentiation scheme is used for all the equations (i.e. momentum, energy and turbulence). The Central Difference (CD) scheme is also tested for comparison.

3.2 Turbulence modelling

Impinging jets are a recommended test for the evaluation of CFD models because they present peculiar turbulent structures particularly difficult with the assumptions taken by the most common turbulence models, as discussed in [16]. In this work four different turbulence models are tested as implemented in the commercial code Star-CD 4.08. All

models are used in their low-Re form (i.e. no wall function), accordingly the mesh is generated so as to accurately resolve the boundary layer as described in 3.1.2.

3.2.1 k-ε model (standard)

A basic assumption is that the dissipative effect of turbulence can be accounted for with a scalar isotropic property called turbulent viscosity μ_t (Bousinnesq approximation). Turbulent viscosity is calculated locally in the computational domain and is related to the local turbulent length and velocity scales. The production terms in the transport equation of turbulent quantities are related to the local gradients of the mean flow.

The k-ε model results from the implementation of the assumption above. In this model μ_t is derived from the turbulent kinetic energy k and the turbulent dissipation rate ε. Transport equations for these two quantities (k and ε) are resolved along with the momentum and energy equations.

The equation for the turbulent kinetic energy, k, is as follows

$$\frac{\partial}{\partial t}(\rho k) + \frac{\partial}{\partial x_j}\left[\rho \overline{u_j} k - \left(\mu + \frac{\mu_t}{\sigma_k}\right)\frac{\partial k}{\partial x_j}\right] = \mu_t\left(2S_{ij}\frac{\partial \overline{u_i}}{\partial x_j}\right) - D_k$$

with

$$S_{ij} = \frac{1}{2}\left(\frac{\partial \overline{u_i}}{\partial x_j} + \frac{\partial \overline{u_j}}{\partial x_i}\right)$$

$$\mu_t = f_\mu \frac{C_\mu \rho k^2}{\varepsilon}$$

$$f_\mu = [1 - e^{-0.0198 Re_y}]\left(1 + \frac{5.29}{Re_y}\right)$$

$$Re_y = \frac{y\sqrt{k}}{\upsilon}$$

$$\mathrm{D_k} = \rho\varepsilon$$

The equations for the turbulent dissipation rate ε for the k-ε model is the following

$$\frac{\partial}{\partial t}(\rho\varepsilon) + \frac{\partial}{\partial x_j}\left[\rho u_j \varepsilon - \left(\mu + \frac{\mu_t}{\sigma_\varepsilon}\right)\frac{\partial \varepsilon}{\partial x_j}\right] = C_{\varepsilon 1}\frac{\varepsilon}{k}\left[\mu_t\left(2S_{ij}\frac{\partial u_i}{\partial x_j} + P'\right)\right] + C_{\varepsilon_2}\left(1 - 0.3e^{-R_t^2}\right)\rho\frac{\varepsilon^2}{k} + C_{\varepsilon_4}\rho\varepsilon\frac{\partial u_i}{\partial x_i}$$

with

$$P' = 1.33\left[1 - 0.3e^{-R_t^2}\right]\left[2S_{ij}\frac{\partial u_i}{\partial x_j} + 2\frac{\mu}{\mu_t}\frac{k}{y^2}\right]e^{-0.00375 Re_y^2}$$

Table 1

Coefficients for the k-ε turbulence model

C_μ	σ_k	σ_ε	$C_{\varepsilon 1}$	$C_{\varepsilon 2}$	$C_{\varepsilon 4}$
0.09	0.75	1.15	1.15	1.9	-0.33

A complete description of the k-ε model can be found in [13].

The k-ε model belongs to the family of the two-equations models. These models are called so because they solve turbulence with two equations. A rather extensive study of two-equations models applied to impinging jets is presented in [17]. The general conclusion of the study is that this type of models is not particularly suitable to solve impinging jet flows. In the same work, the specific results for impinging jets with characteristics similar to the present study indicate that the standard k-ε model performs best. Moreover, the k-ε model is the most popular of the turbulence models used in industry. For these reasons this model is considered in this investigation.

3.2.2 V2F model

The pressure strain affects the turbulent structures in the near wall region of an impinging jet. The V2F model differs from the k-ε model in that it solves for two extra quantities, the wall normal Reynolds stress v^2, and f_{22}, which is an equation for the redistribution of v^2. The V2F model automatically detects the presence of a wall and accounts for its effect on the turbulence.

The k equation in the V2F model is as for the standard k-ε model, the ε equation is

$$\frac{\partial}{\partial x_j}\left[\rho\overline{u_j}\varepsilon - \left(\mu + \frac{\mu_t}{\sigma_\varepsilon}\right)\frac{\partial \varepsilon}{\partial x_j}\right] = \frac{C_{\varepsilon_1}^z}{T_s}\left[\mu_t\left(2S_{ij}\frac{\partial \overline{u_\iota}}{\partial x_j}\right)\right] - \frac{C_{\varepsilon_2}}{T_s}\rho\varepsilon$$

The v^2 equation is

$$\frac{\partial}{\partial x_j}\left[\rho\overline{u_j}v^2 - \left(\mu + \frac{\mu_t}{\sigma_k}\right)\frac{\partial v^2}{\partial x_j}\right] = \rho k f_{22} - 6\rho v^2\frac{\varepsilon}{k}$$

The f_{22} equation is

$$L^2\nabla^2 f_{22} - f_{22} = \frac{1 - C_1}{T_s}\left(\frac{2}{3} - \frac{v^2}{k}\right) - C_2\frac{\mu_t 2S_{ij}\frac{\partial \overline{u_\iota}}{\partial x_j}}{\rho k} - 5\frac{v^2/k}{T_s}$$

With

$$L = C_L\sqrt{max\left(\frac{k^3}{\varepsilon^2}, C_\eta^2\left(\frac{v^3}{\varepsilon}\right)^{1/2}\right)}$$

$$T_s = max\left[\frac{k}{\varepsilon}, C_{kT}\left(\frac{\upsilon}{\varepsilon}\right)^{1/2}\right]$$

$$\mu_t = \rho C_\mu v^2 T_s$$

$$C_{\varepsilon_1}^z = 1 + 0.045\sqrt{k/v^2}$$

Table 2

Coefficients for the V2F turbulence model

C_μ	σ_k	σ_ε	$C_{\varepsilon 1}$	$C_{\varepsilon 2}$	C_1	C_2	C_L	C_η	C_{kT}
0.22	1.0	1.3	1.4	1.9	1.4	0.3	0.23	70.0	6.0

3.2.3 LES (Large Eddy Simulation)

In a turbulent flow it is possible to make a distinction between the turbulent structures, or eddies, according to their size. The largest eddies are often well recognizable structures in the mean flow, these structures extract kinetic energy from the mean flow field. The largest eddies size is in the order of the geometry and its time scale in the order of the mean flow, consequently to assume them as isotropic is a coarse simplification. The energy collected in the large eddies is passed down to smaller and smaller eddies. In this cascade it becomes more and more difficult to distinguish the turbulent structures and the isotropic assumption becomes more representative. In the smallest eddies the energy is dissipated by viscous effects and goes to increment the flow internal energy (heat).

The basic idea behind LES models is to resolve the largest turbulent scales. Consequently, it is necessary to run a three-dimensional, time-dependent computation with a mesh fine enough to resolve the large eddies. Figure 7 is a good example of the resolution of large eddies. The effects of eddies with smaller length scales are accounted for with a sub-grid model. The different LES models differ in how the small eddies are modelled. In this work we use the Smagorinsky model because it is the simplest and most commonly used.

The Navier-Stokes equations for the LES model are:

$$\frac{\partial \overline{u_\iota}}{\partial t} + \overline{u_j}\frac{\partial \overline{u_\iota}}{\partial x_j} = -\frac{1}{\rho}\frac{\partial \bar{p}}{\partial x_i} + \frac{\partial \tau_{ij}}{\partial x_j}$$

The convection term filtered out in the previous equation needs to be model. This is done with the sub-grid scales (SGS) stresses

$$\tau_{ij} = \overline{u_\iota}\,\overline{u_j} - \overline{u_\iota u_j}$$

The Smagorinsky model defines

$$\tau_{ij} - \frac{1}{3}\tau_{kk}\delta_{ij} = 2C_{s2}\Delta^2|\bar{S}|S_{ij}$$

with

$$\bar{S} = \sqrt{2S_{ij}S_{ij}}$$

where $\Delta = cell\ volume^{1/3}$ and C_{s2} is 0.165^2. The equations for k and ε in the sub-grid model are

$$k_{SGS} = 2C_I\Delta^2\bar{S}^2$$

with C_I is set to 0.202.

3.2.4 DES (Detached Eddie Simulation)

In the near wall regions the largest turbulent structures are relatively small. Their size is indeed in the order of the turbulent boundary layer thickness. The boundary layer effects are very important and they need to be accurately accounted for. This leads to a very high computational effort when using LES models. These difficulties lead to the use of a hybrid method called DES. In this type of models the main flow is resolved with the LES approach while the near wall region is modelled with a RANS models. The RANS model chosen in this study is the standard k-ε described in section 3.2.1.

The switch between LES and RANS models is handled locally comparing the cell size with the eddy length scale.

$$\tilde{l} = min\left(\frac{k^{3/2}}{\varepsilon}, C_{DES}\max(\Delta_x, \Delta_y, \Delta_z)\right)$$

with Δ_x representing the cell size.

The switch acts on the dissipative source for the *k* equations as follows:

$$\mathrm{D_k} = \rho\frac{k^{3/2}}{\tilde{l}}$$

4 Transient modelling results and discussion

4.1 Simulation results

All simulations are run for 200s simulated time and the averaging for post-processing is done on the last 100s. To check the statistical relevance of this average, a case is run for a longer period and no significant difference is detected. The results are presented as the average calculated for constant radii. The quantities describing the turbulence in the jet flow are normalized with the jet bulk velocity at the nozzle outlet W_b.

4.2 Results from LES simulations

4.2.1 Mesh size effects

Two different mesh topologies are tested with the same number of cells but a different distributions. Both meshes are identical for z/D < 0.5. The default mesh “mesh 1” has a constant cell size in the jet direction for 0.5 < z/D < 6. “mesh 2” grows geometrically

from the impingement wall to the upper boundary (resulting in aspect ratio of ca. 5 at the inlet).

Figure 8 a) shows the effect of cell size on the turbulent fluctuations near the inlet. With mesh 2 the cells are too big to resolve these fluctuations and they are dampened, consequently the level of turbulence is under predicted. The same picture shows how the fluctuations are better resolved with mesh 1 being the resolved k of the same order of "k pipe" (k for fully developed pipe flow).

Figure 8 b) shows the modelled turbulent kinetic energy k computed for the sub grid model. In the region at r/D = 0,5 there is a strong velocity gradient between the jet exiting from the nozzle and the quiescent fluid. This works in the k equation resulting on a peak in the modelled k.

At z/D = 0,5 the cell size is alike for the two cases. Figure 8 c) shows that the resolved k has similar values for both meshes in particular for r > D/2. Notably, in the shear layer the levels of k that are almost one order of magnitude higher than at the inlet.

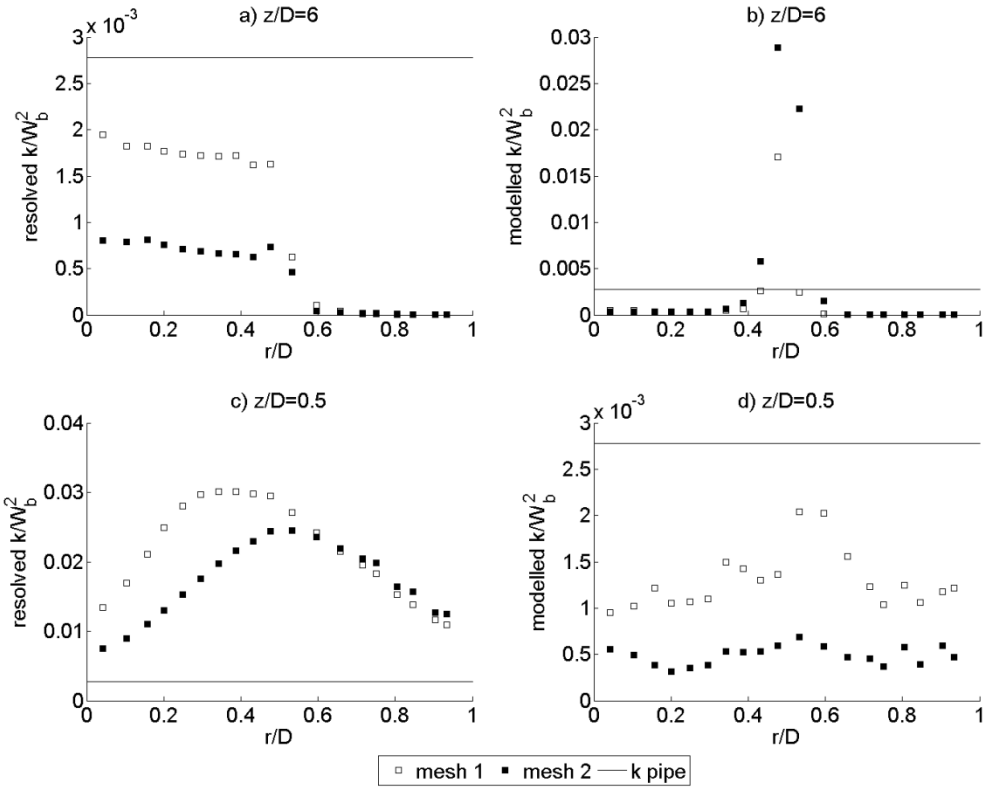

Figure 8. Effects of mesh topology on resolved and modelled k. For comparison "k pipe" is included which is the turbulence kinetic energy expected in a fully developed flow in a straight pipe at the same Re.

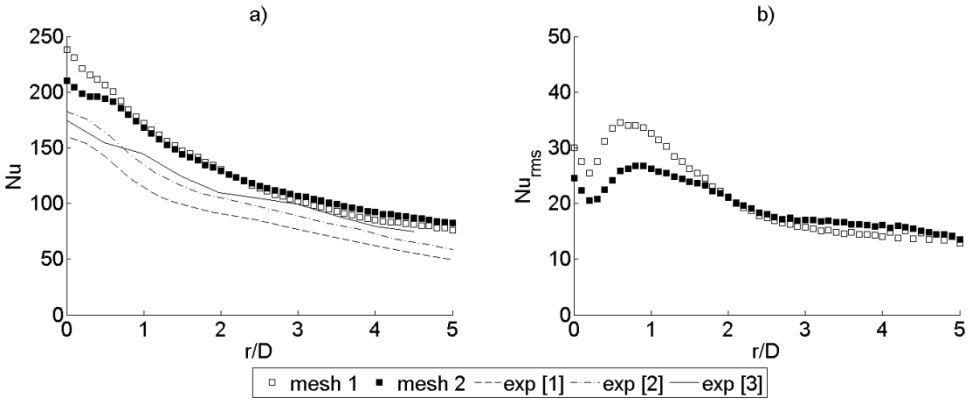

Figure 9. Effect of mesh topology on Nu and Nu_{rms}.

4.2.2 Effects of the numerical discretization

Tree cases are run with values for the MARS parameter of 0, 0,25 and 0,5 (see section 3.1.5). A low value for the parameter gives a more robust but less accurate solution and vice versa. At the first cell layer (Figure 10 a) and b)) there are no relevant differences between the cases. Further downstream (Figure 10 c) and d)) a low value for the MARS parameter dampens the resolved turbulence fluctuations. The same effect can be seen also on the Nusselt number fluctuations (Nu_{rms}) in Figure 11 b). On the other hand no sensible difference is appreciate on the average Nu (Figure 11 a)).

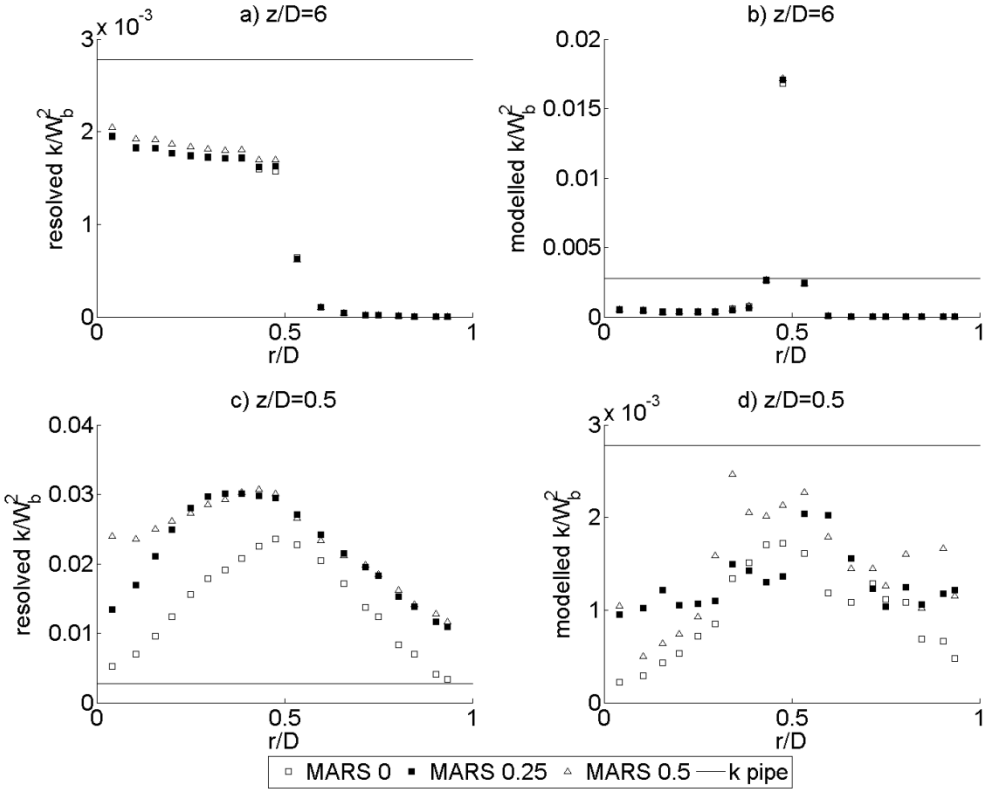

Figure 10. Effects of differentiating scheme on resolved and modelled k.

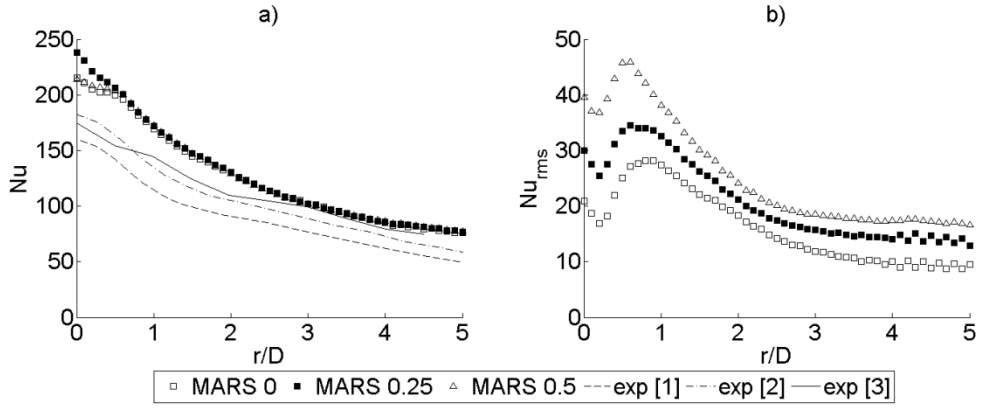

Figure 11. Effect of differentiating scheme on Nu and Nu_{rms}.

In the literature, use of the CD scheme is recommended for LES simulations at least for the momentum equations. A few attempts to apply this scheme gave no good results generating unphysical values of Nu.

4.2.3 Effect of inlet turbulence

Two cases are run respectively with four times lower and higher inlet resolved turbulent kinetic energy k. Figure 12 shows the effect of the inlet boundary condition at z/D=0,5 the fluctuations are of similar magnitude in all cases. The level of turbulence here is much higher than at the inlet and depends mainly on the turbulence generate in the shear layer. Consequently the inlet turbulence level has not effects on the average Nu outside the impingement region (Figure 13 a). In the impingement region (r/D<0,5) the results differ for some 15% between each other. However, these do not follow a proportional correlation between increasing inlet turbulence and increasing Nu. A correlation can be notice between the Nu (Figure 13 a)) and the modelled turbulent kinetic energy in the proximity of the wall (Figure 12 d)) suggesting that this parameter is more important than others.

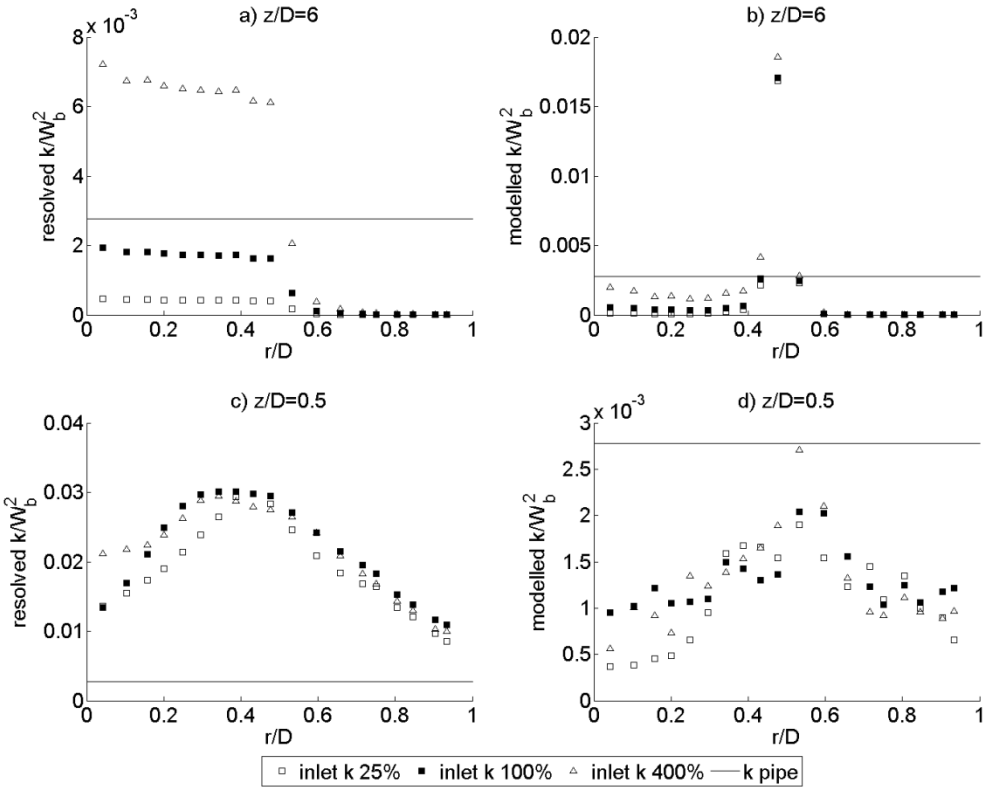

Figure 12. Effects of inlet turbulence on resolved and modelled k.

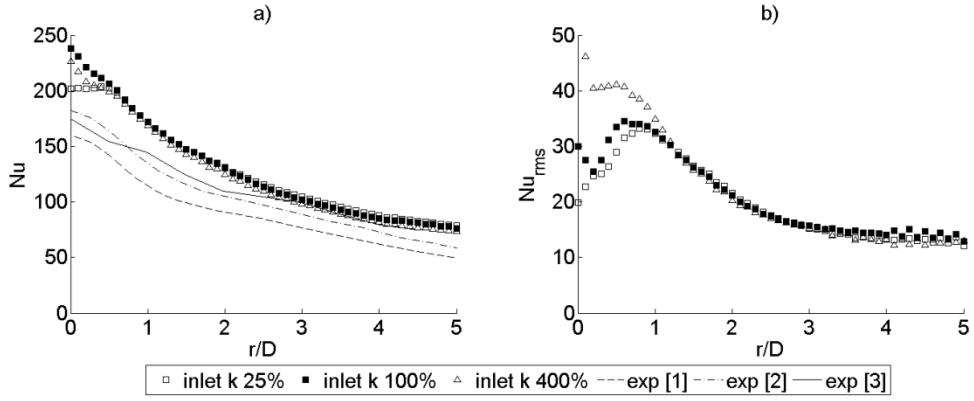

Figure 13. Effect of inlet turbulence on Nu and Nu_{rms}.

4.2.4 Resolved k vs. measurements

The LES simulations well capture the magnitude of both the velocity magnitude and the radial velocity fluctuations u'_{rms}. The largest discrepancies are noticeable close to the wall. The discretization order has a strong influence on the results, Figure 14 b) shows that the simulations run with growing values for the MARS scheme parameter result in larger fluctuations near the wall.

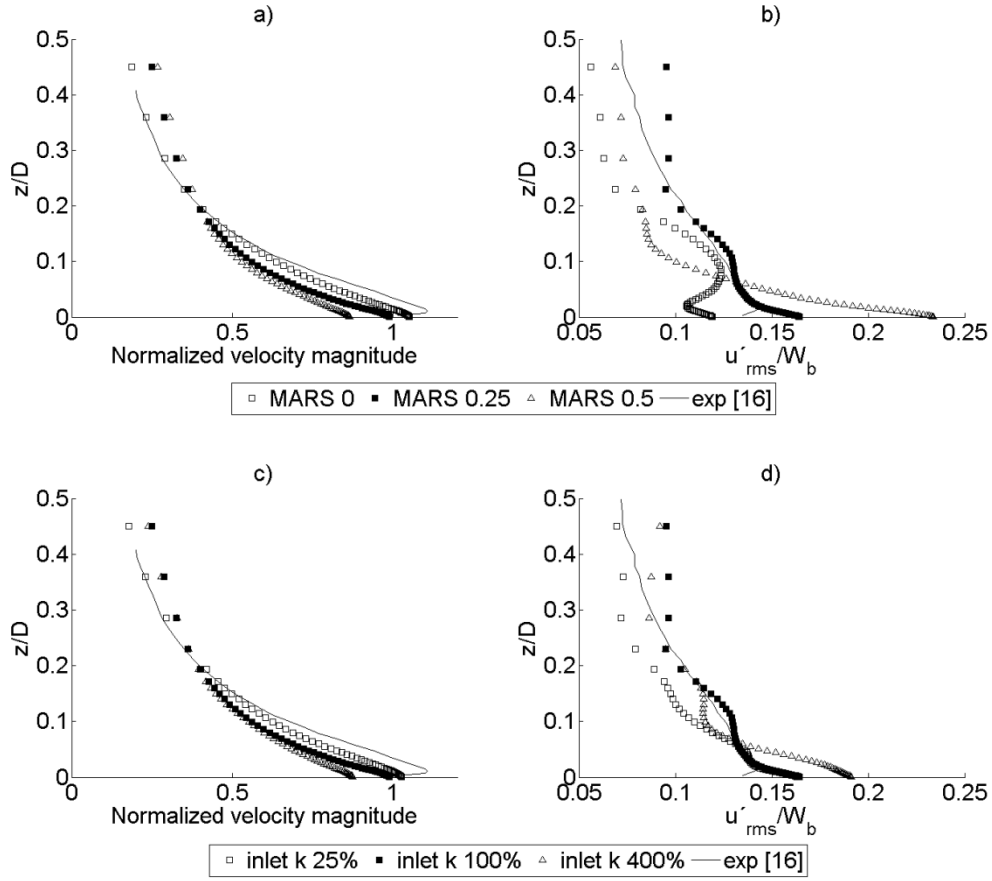

Figure 14. Velocity magnitude and radial velocity fluctuation (u_{rms}) at r/D = 1.

4.3 Heat transfer, comparison between LES, DES, k-ε and V2F

Simulations are performed to cross compare the different turbulence models presented in chapter 3. The different models are compared based on their prediction of the heat transfer between the jet and the wall.

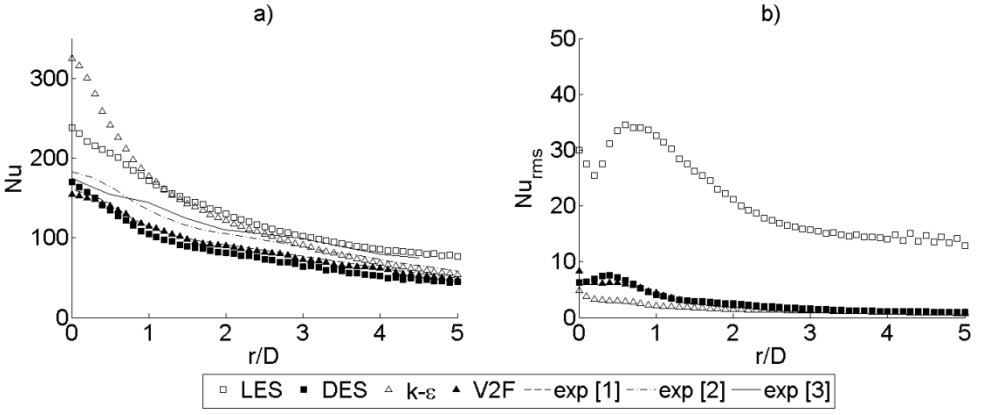

Figure 15. Effect of turbulence model on the Nu.

Figure 15 a) shows the average Nusselt number predicted by different turbulence models. As expected, the k-ε model over-predicts the Nu at the stagnations point getting closer to the measured one only for higher r/D. The V2F model slightly under predicts the Nu over the entire range of r/D. The DES model show results very similar to the V2F in almost the entire range of r/D. The LES model over predicts the experimental results in the entire range of r/D's and this is the case for all the tests done with this model as presented in the previous sections.

The LES model predicts the Nu_{rms} to be 10-15% of the average Nu at the stagnation (see Figure 15 b)). This correlates well with the data presented in [5]. The other turbulence models under predict the Nusselt number fluctuations. This behavior is expected from the k-ε and V2F models in which turbulent fluctuations are very much dampened. On the other hand, a similar behavior is shown even for the DES model, even though this model should resolve the fluctuations similarly to the LES model.

The results regarding the Nu_{rms} can be further explained considering how turbulence is resolved by the different models upstream the impingement wall (Figure 16). The LES model resolves the major part of the turbulent velocity fluctuations. All other models do not capture the fluctuations, the turbulence is modelled instead. The DES model shows characteristics very similar to the k-ε and V2F model indicating that it is working in RANS mode. At r/D = 0 the modelled k is very similar between the DES and the k-ε model but this does not find match with the result about the Nu presented in Figure 15 a).

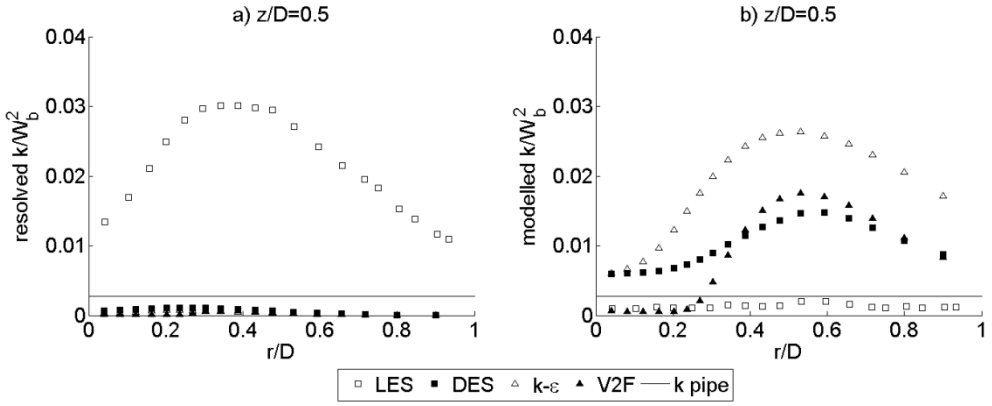

Figure 16. Resolve and modelled turbulence in the vicinity of the impingent wall, comparison of different turbulence models.

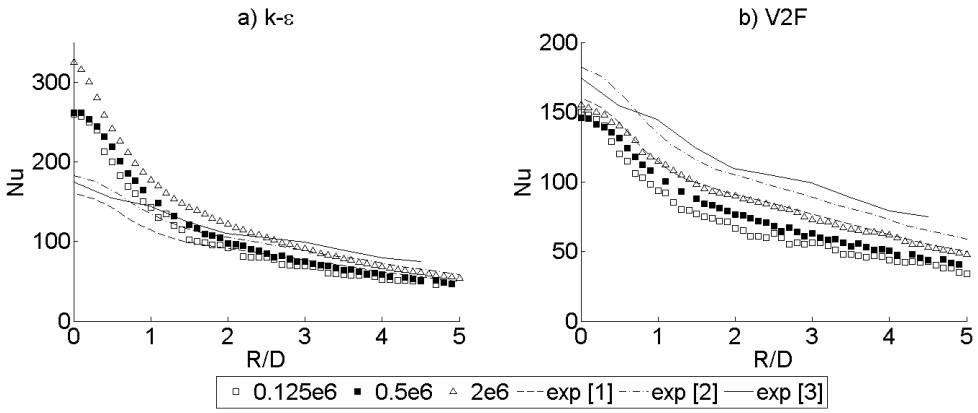

Figure 17. Effect of mesh density on the Nu.

The effect of the mesh density for the k-ε and V2F model can be seen in Figure 17. Three different meshes are tested with 0.125e6, 0.5e6 and 2e6 cells. The k-ε model does not perform well particularly in the impinging region. It can be also noted that this model performs the worst with the higher mesh density. A possible source of the difference between these results is that only the simulations with 2e6 cells are carried out applying the synthetic fluctuations at the inlet. However, considering Figure 12, this should not have a significant influence. The V2F model slightly under predicts the level of Nusselt number in the entire range, giving quite satisfactory results, particularly with the finest mesh.

4.4 Computational cost

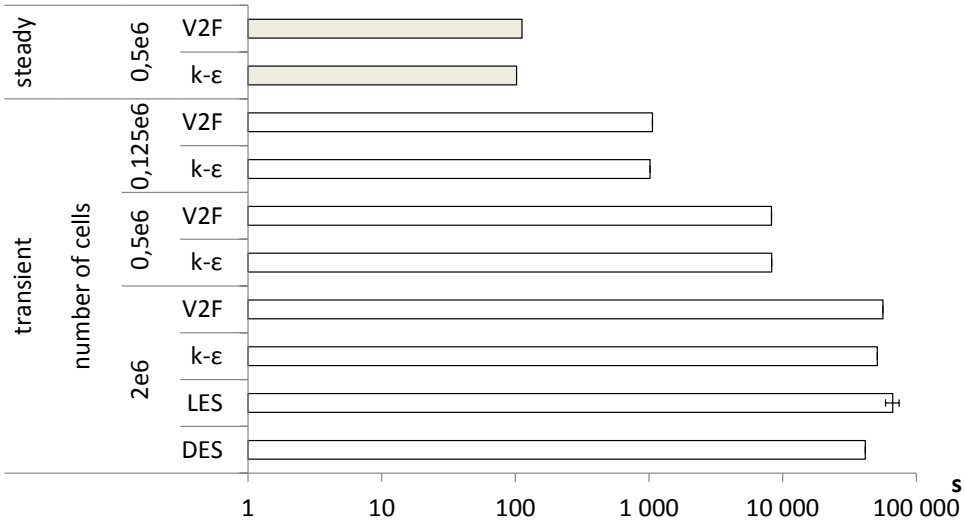

Figure 18. CPU time per simulated second. More than one simulation is run with the LES model, the error bar is the standard deviation.

Figure 18 presents the time necessary for one CPU to compute one second of simulated time. This time is affected by many factors such as the number and type of CPUs used. Another important factor is the need to solve extra subroutines. These are for example the two extra subroutines used for the implementation and post processing of the synthetic

fluctuation. In parallel computing, communication between CPUs is a significantly time-consuming process. The domain is partitioned in clusters of cells and each cluster is assigned to a CPU. At the end of each iteration, the solution at the cluster boundaries needs to be passed to the CPU(s) computing for the adjacent cell(s).

For the reasons presented above, the data from Figure 18 can be treated only as something indicative, since different types of CPUs were used, as well as different partitions. It can be noticed that the V2F is slightly slower than the k-ε model. This is probably due to the fact that the V2F model solves for two extra equations. Six simulations with the LES model are run with the same CPU configuration. The standard deviation for the runtime of these simulations is about 11%, as shown in the error bar in Figure 18. The DES model is relatively fast compared with the other ones tested; further study is however necessary to better access this model since in this study only one simulation is run with it. In Figure 18 the computational cost related to the growing number of cells can also be appreciated. The same figure also shows the computation time for steady state simulations for comparison.

5 Conclusions

The objective of this work is to evaluate different approaches to the simulations of impinging jets. The test and cross-evaluation of several different models is useful when deciding how to address this kind of flow.

Considering turbulence models, the k-ε model is verified to be not sufficiently accurate in predicting heat transfer. The V2F model is slightly more computationally expensive but gives significantly better results, even with a relatively coarse mesh. The V2F model slightly under predicts the heat transfer compared to the experimental results. The DES model gives results very similar to the V2F model and should be considered for simulations of this kind, although it must be mentioned that this model is studied only briefly in this work. Furthermore, the results from the heat transfer fluctuations indicate that the k-ε, the V2F and the DES models do not capture the transient dynamic of the flow. In other words, they act much like their respective steady state simulation.

The LES model is studied more extensively, changing a number of parameters. This model is capable of resolving the turbulent structures in the shear layer in a satisfactory manner. The results are good both in terms of heat transfer prediction and flow-field turbulent characteristics. Only relatively little differences are noted when changing the various parameters. The only exception is the CD equation discretization scheme, the use of which gives adversely affected the predicted heat transfer. In general, the LES turbulence model over predicts heat transfer, compared with the experimental measurements. Unfortunately, this method is inherently expensive, since it requires both a fine mesh and a transient simulation, exponentially increasing the computational cost.

Using the LES model it is possible to verify that inlet turbulent fluctuations play only a minor role in the heat transfer phenomenon compared to the turbulence produced in the shear layer. This is true at least for the nozzle-to wall distance z/D studied in this work.

Nowadays, numerical simulations are used to study the combustion chambers of internal combustion engines. To date, most such simulations have focused on the combustion process. However, for many reasons, there is a growing need to consider the thermal interaction with combustion chamber walls. The results presented in this work will be used as a reference in order to improve the ability of ICE simulations to accurately account for heat transfer effects.

References

1. Baughn, J. W. and Shimizu, S. [1989], Heat transfer measurements from a surface with uniform heat flux and an impinging jet, ASME J. Heat Transfer 111/1097.
2. Katti, V.and Prabhu, S.V. [2008], Experimental study and theoretical analysis of local heat transfer distribution between smooth flat surface and impinging air jet from a circular straight pipe nozzle, Int. J. Heat Mass Transfer article in press.
3. Lytle, D. and Webb, B.W. [1994], Air jet impingement heat transfer at low nozzle plate spacings, Int. J. Heat Mass Transfer 37 1687–1697.

4. Gao, N., Sun H. and D. Ewing [2003], Heat transfer to impinging round jets with triangular tabs, Int. J. Heat Mass Transfer 46 2557–2569.
5. O'Donovan T. S. and Murray D. B. [2007], Jet impingement heat transfer – Part I: Mean and root-mean-square heat transfer and velocity distributions, Int. J. Heat and Mass Transfer 50 3291–3301.
6. O'Donovan T. S. and Murray D. B. [2007], Jet impingement heat transfer – Part II: A temporal investigation of heat transfer and local fluid velocities, Int. J. Heat and Mass Transfer 50 3302–3314.
7. Yue-Tzu Yang, Shiang-Yi Tsai [2007], Numerical study of transient conjugate heat transfer of a turbulent impinging jet. Heat and Mass Transfer 50 799–807.
8. Gao N. and Ewing D. [2006], Investigation of the effect of confinement on the heat transfer to round impinging jets exiting a long pipe, Int. J. of Heat and Fluid Flow 27 33–41
9. Koseoglu M.F. and Baskaya S. [2007], The effect of flow field and turbulence on heat transfer characteristics of confined circular and elliptic impinging jets, Int. J. of Thermal Sciences article in press.
10. Viskanta R. [1993], Heat transfer to impinging isothermal gas and flame jets. Experimental Thermal and Fluid Science 6:111-134
11. K. Jambunethan, E. Lai, M. A. Moss and B. L. Button [1992], A review of heat transfer data for single circular jet impingement, Int. J. Heat and Fluid Flow, Vol. 13, No. 2 106-115
12. L. Davidson [2007], Using isotropic synthetic fluctuations as inlet boundary conditions for unsteady simulations. Advances and applications in Fluid Mechanics, Vol. 1 Issue 1 1 - 35
13. Lien, F.S., Chen, W.L. and Leschziner, M.A. [1996], Low-Reynolds-Number Eddy-Viscosity Modelling Based on Non-linear Stress-Strain/Vorticity Relations, Proc. 3rd Symp. on Engineering Turbulence Modelling and Measurements, Crete, Greece.
14. M. Angioletti a, E. Nino a, G. Ruoccob, CFD turbulent modelling of jet impingement and its validation by particle image velocimetry and mass transfer measurements, International Journal of Thermal Sciences 44 (2005) 349–356
15. M. Bovo et al, On the numerical modelling of impinging jet heat transfer, Int. Symp. on Convective Heat and Mass Transfer in Sustainable Energy, 2009, Tunisia
16. Cooper, D., Jackson, D. C., Launder, B. E. & Liao, G. X. 1993 Impinging jet studies for turbulence model assessment-I. Flow-field experiments. Int. J. Heat Mass Transf. 36, 2675–2684.
17. H. M. Hofmann, R. Kaiser, M. Kind, H. martin, Calculations of steady and pulsating impinging jets—an assessment of 13 widely used turbulence models, Numerical heat transfer, part b, 51: 565–583, 2007.
18. Thomas Hällqvist 2006, Large Eddy Simulation of Impinging Jets with Heat Transfer KTH Mechanics, SE-100 44 Stockholm, Sweden, dissertation thesis.
19. Tobias Husberg, Savo Gjiria and Ingemar Denbratt, Piston Temperature Measurements by use of thermographic phosphors and thermocouples in a heavy-duty diesel engine run under partially premixed conditions, SAE 2005-01-1646